*Supplementary Information*

1. **NMR data acquisition.**
2. **NMR relaxation data analysis**
3. **Error Analysis**
4. **PARASHIFT quantification of T and pH, and error analysis**

5. **ESI Fig 1** (*Left*) Illustration of experimental array, in a Teflon holder, using 5 equimolar solutions of buffered **[Tm.L$^1$]** at different pH values shown and with de-ionised $H_2O$ in the centre (0.1 M MOPS, 1.2 mM, $H_2O$). (*Middle*) Phantom image at the $H_2O$ offset (-618 Hz, intensity scale 0-4000 a.u.). (*Right*) Phantom image at the **[Tm.L$^6$]** *tert*-butyl offset (18284 Hz, intensity scale 0-0.1 a.u.), both: TR = 23.6 ms; TE= 1.2 ms; nt = 4 ($H_2O$), 80 (*tert*-butyl); SW = 6000 Hz; spectral points 128; Matrix 16 x 16; FOV 40 x 40; slice thickness 8 mm; T = 310 K).
6. **ESI Figure 2** Spectral analysis from CSI image of **[Tm.L$^1$]**, showing the frequency detected for each ROI peak for: pH 6.2 (purple), 3037 Hz; 6.6 (yellow); 7.1 (blue); 7.5 (green); and 8.1 (red), 2893 Hz. Total shift = -144 Hz = 0.48 ppm, offset frequency = 18284 Hz, TR = 23.5ms, TE = 1.2ms, nt = 80, slice thickness = 8 mm, 128 spectral points, 6010 spectral width, T = 310 K.
7. **ESI Fig 3** Variable temperature study of [Tm.HL$^1$]$^-$, and the parent analogue.
8. **ESI Fig 4** Variation of the chemical shift with temperature, for the t-butyl resonance in the two main isomeric species of [Tm.HL]$^-$

## 1. NMR data acquisition

$^1$H spectra were obtained at 295 K (unless stated otherwise) on Varian spectrometers operating at 4.7, 9.4, 11.7, 14.1, 16.5 Tesla, specifically on a Mercury 200 spectrometer ($^1$H at 200.057 MHz), a Mercury 400 spectrometer ($^1$H at 399.97 MHz), a Varian Inova-500 spectrometer ($^1$H at 499.78 MHz), a Varian VNMRS-600 spectrometer ($^1$H at 599.944 MHz) and a Varian VNMRS-700 spectrometer ($^1$H at 700.000 MHz). Commercially available deuteriated solvents were used. Measurements at 1T ($^1$H at 42.5MHz) were made on a Magritek Spinsolve spectrometer. Samples were inserted at 295K and $T_1$ measurements were made over the range 295-301K, using the temperature dependence of the t-Bu shift ($1/T^2$ dependence) to estimate the measurement temperature.

The operating temperature of the spectrometers was measured with the aid of an internal calibration sample of neat ethylene glycol. The recorded free induction decays were processed using backward linear prediction, optimal exponential weighting, zero-filling, Fourier transform, phasing and baseline correction (by Whittaker smoothing), if necessary.

## 2. NMR relaxation data analysis

The nuclear relaxation times of the nuclei of interest were measured at the 6 different fields mentioned above. The $T_1$ values were measured using the inversion-recovery technique. At first a crude $T_1$ value was obtained, which was then used as the initial guess in multiple repeat experiments. The incremented delay time was set to show full inversion and full recovery to equilibrium of the signal, which is roughly achieved at five times the $T_1$ value. The concentration of a sample was kept constant throughout a series of measurements, which was in the range of 0.1 to 1 mM.

The measured nuclear relaxation data were fitted by using a modified Matlab algorithm originally written by Dr. Ilya Kuprov of Southampton University. The algorithm uses the Solomon-Morgan-Bloembergen equation (1) to fit the measured relaxation data using the Matlab internal Levenberg-Marquardt minimisation of the non-linear squares error function. The results were analysed iteratively. It was assumed that longitudinal and transverse electronic relaxation times were of a similar magnitude.

$$R_1 = \frac{2}{15}\left(\frac{\mu_0}{4\pi}\right)^2 \frac{\gamma_N^2 g_{Ln}^2 \mu_B^2 J(J+1)}{r^6}\left[3\frac{T_{1e}}{1+\omega_N^2 T_{1e}^2} + 7\frac{T_{1e}}{1+\omega_e^2 T_{1e}^2}\right] + \frac{2}{5}\left(\frac{\mu_0}{4\pi}\right)^2 \frac{\omega_N^2 \mu_{eff}^4}{(3k_B T)^2 r^6}\left[3\frac{\tau_r}{1+\omega_N^2 \tau_r^2}\right] \quad (1)$$

## 3. Error Analysis for Relaxation Measurements

Each relaxation measurement was repeated at least three times and the mean value recorded. The number of transients used in the measurements was determined by the signal-to-noise ratio and also by the linewidth of the resonance of interest. In each case, the signal was fully recovered during the inversion-recovery sequence.

A statistical error analysis was undertaken to determine the fitting errors. The experimental errors of the measured relaxation rates were combined and used to perturb the relaxation rates for each complex at each field. These perturbed rates together with the unperturbed relaxation rates were used in a statistical error analysis to obtain the error values for the individual parameters ($\mu_{eff}$, $\tau_r$ and $T_{1e}$).

## 4. PARASHIFT quantification of T and pH.

Quantification of tissue temperature and pH was carried out using spectral analysis of the 2DSI data to measure the peak frequencies of water, $[Dy.HL^1]^-$ and $[Tm.HL^1]^-$. Each 2DSI dataset was first processed using a Hanning spatial apodisation function, zero-filling of the spectral dimension to 4096 points and line-broadening of 100 Hz. The dataset contains spectra across the full spatial distribution of the field of view. Selected spectra from voxels corresponding to liver, kidney and bladder were extracted from the data matrix and peak frequencies determined. In the pre-injection 2DSI dataset, spectra were extracted from the ethylene glycol and PARASHIFT compartments of the phantom to provide reference frequencies at known T and pH.

The spectral offset frequency of the *tert*-butyl resonance ($\omega_t$) can be described mathematically by

$$\omega_t = K(T) + Y(pH) + C \tag{2}$$

where $K(T)$ is a function describing the temperature dependence of the shift, $Y(pH)$ is a function describing the pH dependence of shift and C is a constant. The *in vitro* assessment of temperature dependence shows $K(T)$ has a linear dependence over the range of temperature encountered *in vivo*,

$$K(T) = m_{para} \times T \tag{3}$$

while the pH dependence is sigmoidal in function, described by

$$Y(pH) = \omega_{min} + \frac{(\omega_{max} - \omega_{min}) \times pH^A}{(pH^A + pH_{mid}^A)} \tag{4}$$

with $\omega_{max}$ and $\omega_{min}$ the upper and lower asymptotes of the sigmoidal function, $pH_{mid}$ the point of inflection and $A$ is a constant affecting the slope of the curve.

From these equations, the frequency difference of the *tert*-butyl ($\Delta\omega_t$) resonance between regions of differing T and pH (denoted by the subscripts 1 and 2) can be written as

$$\Delta\omega_t = m_{para}\Delta\mathrm{T} + (\omega_{max} - \omega_{min})\Delta\varepsilon_{pH} \tag{5}$$

and

$$\Delta\varepsilon_{pH} = \frac{pH_2^A}{(pH_2^A + pH_{mid}^A)} - \frac{pH_1^A}{(pH_1^A + pH_{mid}^A)} \tag{6}$$

It should be noted that $A$, $m_{para}$ and $pH_{mid}$ are specific to each agent and so have different values for $[Dy.HL^1]^-$ and $[Tm.HL^1]^-$. Fitting of *in vitro* temperature and pH dependence data allowed all of the constants to be determined experimentally. For $[Tm.HL^1]^-$: $A_{Tm}$= -13.6, $pH_{mid}$ = 7.3, (ωmax - ωmin) = -329.5 Hz and $m_{para}$ =−135 Hz/K, while for $[Dy.HL^1]^-$: $A_{Dy}$= 19.91, $pH_{mid}$ = 7.18, (ωmax - ωmin) = 574.2 Hz and $m_{para}$ = +123 Hz/K.

Separate versions of equations (5) and (6) can then be written for $[Dy.HL^1]^-$ and $Tm.HL^1]^-$ which are linked since the temperature and pH experienced by the two different agents are the same and therefore the equations contain only 2 unknowns (ΔT and ΔpH). Using the two measurements of peak frequency shift relative to the calibration phantom then allows these simultaneous equations to be solved for ΔT and ΔpH, and since the phantom T and pH are known, provides measurements of the absolute tissue T and pH.

As an example, the frequency shifts and calculated pH and ΔT for the animal illustrated in Figure 11 of the main manuscript are given in **Table S1** below.

| Region | Δf Dy (Hz) | Δf Tm (Hz) | pH | ΔT (K) |
|---|---|---|---|---|
| Liver | -81 | 40 | 7.14 | -0.6 |
| Kidney | -95 | 108 | 6.96 | -0.8 |
| Bladder | -461 | 461 | 6.80 | -3.5 |

**Table S1***:* Measured frequency shifts and calculated *in vivo* tissue pH and temperature differences (relative to the external phantom at pH 7.0) in one animal. Spectra are illustrated in Figure 11 of the main manuscript.

Numerical modelling was applied to examine the sensitivity of the calculated pH and ΔT values to the errors in the constants in equations 5 and 6, ($m_{para}$ temperature coefficient of frequency shift, $A$ sigmoidal fitting constant) and to errors in the measured peak frequency. Allowing $m_{para}$ to vary by ±0.01ppm (the error determined from the experimental data, main text figure 8), peak frequency to vary by the spectral resolution in the zero-filled datasets (±7 Hz: see below) and the exponent $A$ by ±0.5 (arbitrary units), the greatest errors in calculated pH and T were 0.33 units and 0.7 C respectively. This

magnitude of error was found at extremes of pH (greater than 8 or less than 6). This observation is consistent with the flattening of the sigmoidal pH versus frequency dependence at extremes of pH as the curve approaches its asymptotes (main text, figure 3). Across the pH range 6 to 8, maximum errors in pH and T were 0.5 units and 0.2 C respectively.

An analysis was conducted of the effect of zero-filling, on the ability to detect changes in the frequency of the spectral peak. We simulated FIDs by calculating signals according to the acquisition parameters used in the in vivo studies. Complex signals were simulated with a spectral width of 60,000Hz, 512 data points sampled and a T2 of 2.5ms. Under these circumstances the acquired (true) spectral resolution is 117.2 Hz. We simulated 100 different FIDs with the spectral peak frequency ranging between -19687.5 and -19746.1 Hz. These frequency limits represent the extreme conditions where the spectral peak frequency is precisely equal to a spectral data point and where the frequency is precisely midway between spectral data points. Each FID was processed applying zero-filling by factors of 1 (none) to 16, followed by FFT and peak peaking, to determine the measured peak frequency ($f_{meas}$). The error in quantifying frequency was then calculated as the absolute difference between the measured and simulated frequency.

The plot below shows the mean error (with error bars indicating the absolute range of error) in quantifying the frequency across the set of spectra for each level of zero filling. As expected when no zero-filling is used, the error ranges from 0 to half of the spectral sampling interval. As progressive levels of zero-filling are applied the error falls mapping to the nominal resolution of the zero-filled spectra.

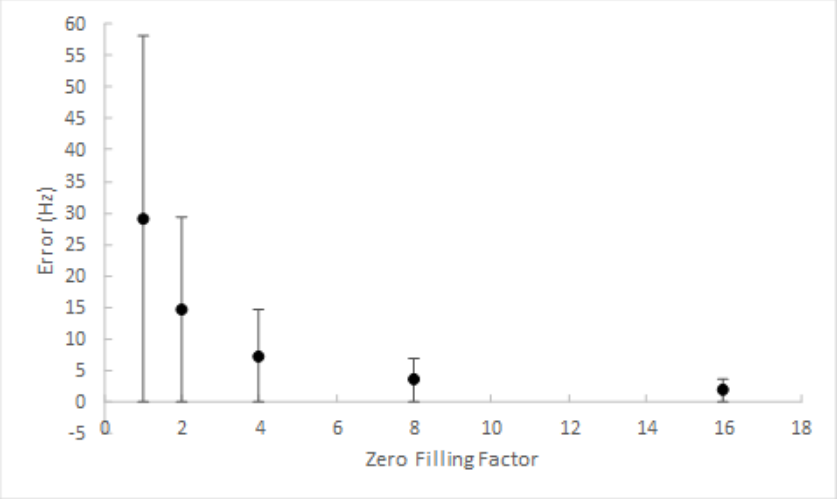


The true spectral resolution of the dataset is determined by the acquisition parameters (sweep width and sampled points), but this data shows that the effect of zero-filling (essentially a sinc interpolation) does allow the frequency of the peak to be determined with an increasing level of accuracy. The in vivo data used zero filling, and used a x8 factor of zero-filling; the above plot confirms that using this approach it does convey the ability to detect signal changes within the 13 Hz range that is quoted. As above, we applied these error data to further numerical modeling, in order to understand the propagation of the frequency uncertainty on assessment of pH and T, and determined that the worst case errors across the pH range 6 to 8, 0.5 units and 0.2 C respectively.

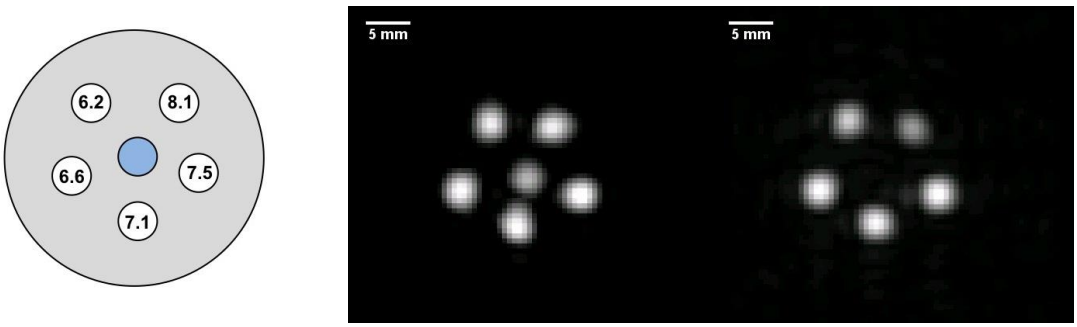


**ESI Figure 1** (*Left*) Illustration of experimental array, in a Teflon holder, using 5 equimolar solutions of buffered **[Tm.L$^{1}$]** at different pH values shown and with de-ionised $H_2O$ in the centre (0.1 M MOPS, 1.2 mM [Ln.HL$^{1}$], $H_2O$). (*Middle*) Phantom image at the $H_2O$ offset (-618 Hz, intensity scale 0-4000 a.u.). (*Right*) Phantom image at the **[Tm.L$^{6}$]** *tert*-butyl offset (18284 Hz, intensity scale 0-0.1 a.u.), both: TR = 23.6 ms; TE= 1.2 ms; nt = 4 ($H_2O$), 80 (*tert*-butyl); SW = 6000 Hz; spectral points 128; Matrix 16 x 16; FOV 40 x 40; slice thickness 8 mm; T = 310 K).

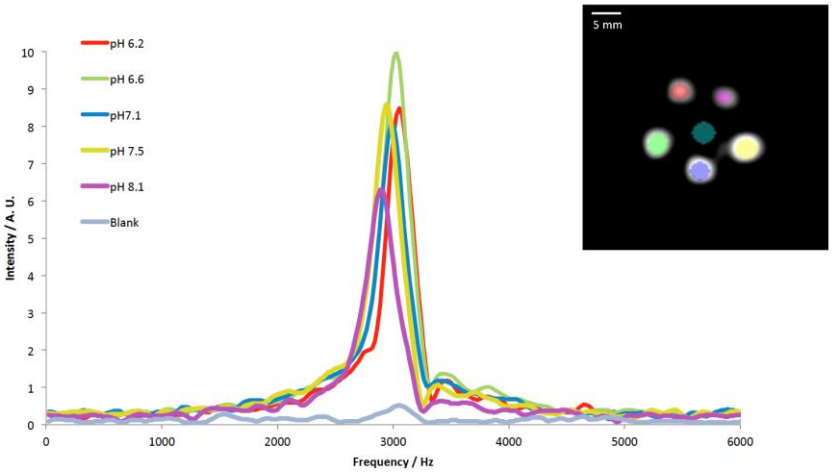


**ESI Figure 2** Spectral analysis from CSI image of **[Tm.L$^1$]**, showing the frequency detected for each ROI peak for: pH 6.2 (purple), 3037 Hz; 6.6 (yellow); 7.1 (blue); 7.5 (green); and 8.1 (red), 2893 Hz. Total shift = -144 Hz = 0.48 ppm, offset frequency = 18284 Hz, TR = 23.5ms, TE = 1.2ms, nt = 80, slice thickness = 8 mm, 128 spectral points, 6010 spectral width, T = 310 K.

***ESI Fig 3*** Variable temperature study of $[Tm.HL^1]^-$, and the parent analogue

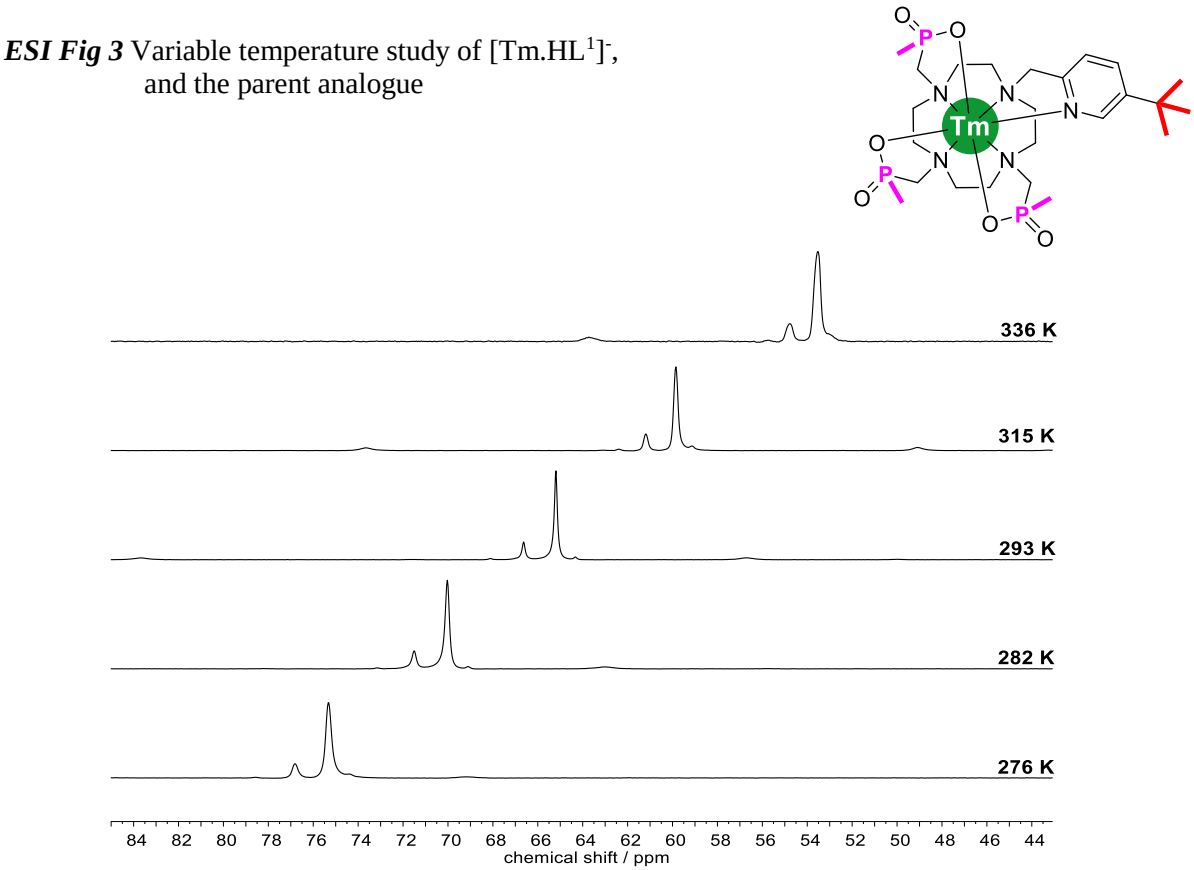


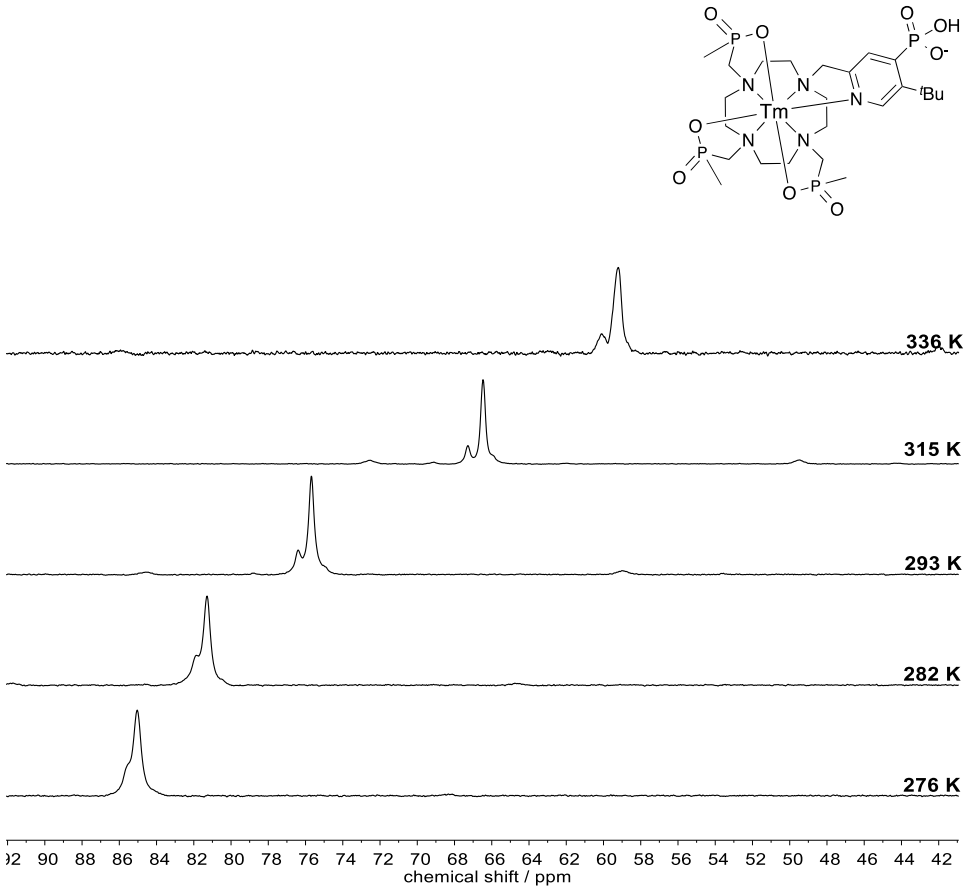


Gradual divergence of signals with increasing temperature, (11.7 T, pD = 7.3)

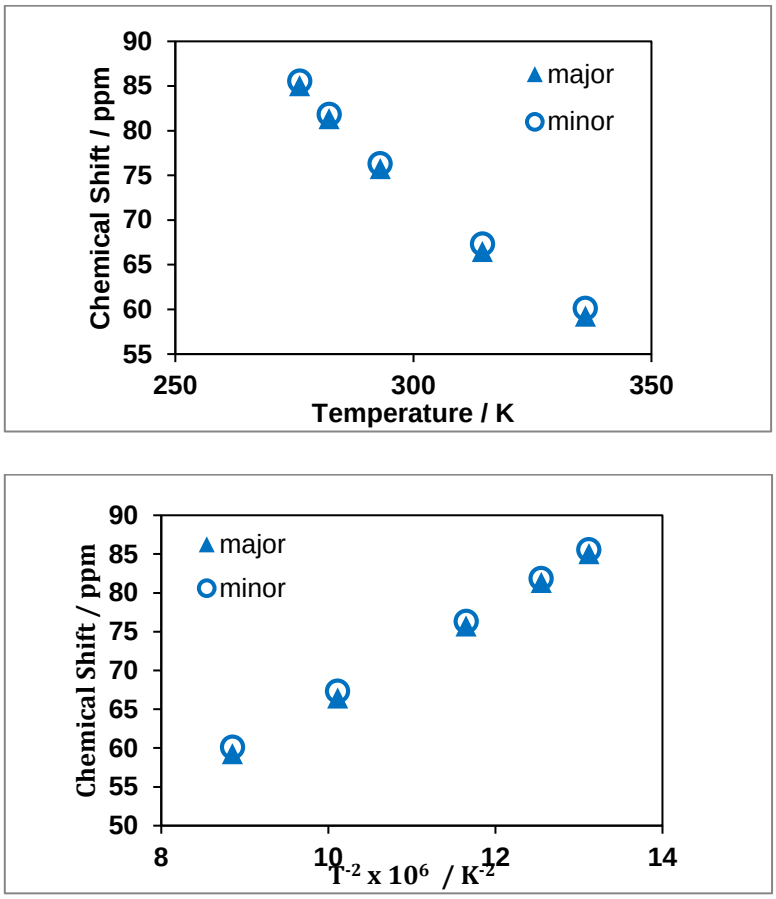


**ESI Figure 4** Variation of the chemical shift with temperature, for the t-butyl resonance in the two main isomeric species of $[Tm.HL]^-$

## 7. Synthesis of Ligand and Lanthanide(III) Complexes

### HPLC purification

The complexes were purified by reverse-phase HPLC at 295 K, using a Shimadzu system consisting of a Degassing Unit (DGU-20$A_{5R}$), a Prominence Preparative Liquid Chromotograph (LC-20AP), a Prominence UV/Vis Detector (SPD-20A) and a Communications Bus Module (CBM-20A). An XBridge C18 OBD 19 x 100 mm, i.d. 5 μM column was used to purify the complexes. A gradient elution with a solvent system composed of $H_2O$ + 0.1% HCOOH/ MeOH + 0.1% HCOOH was performed, for a total run time of 17 min, from 10% (MeOH + 0.1% HCOOH) to 100% (MeOH + 0.1% HCOOH).

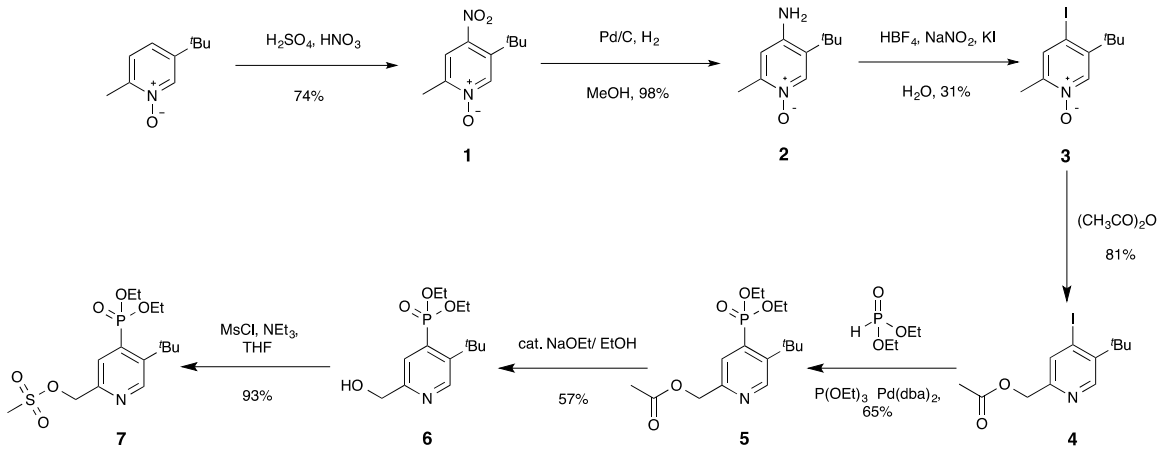


**Scheme 1**

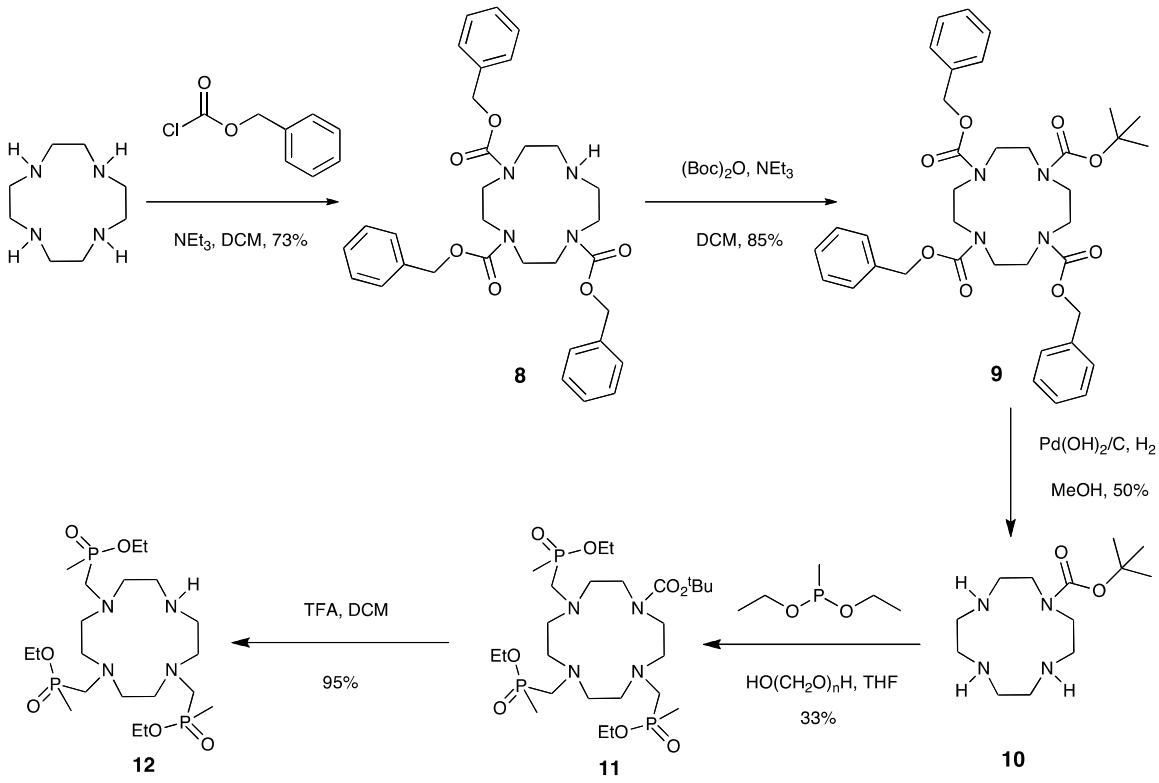


**Scheme 2**

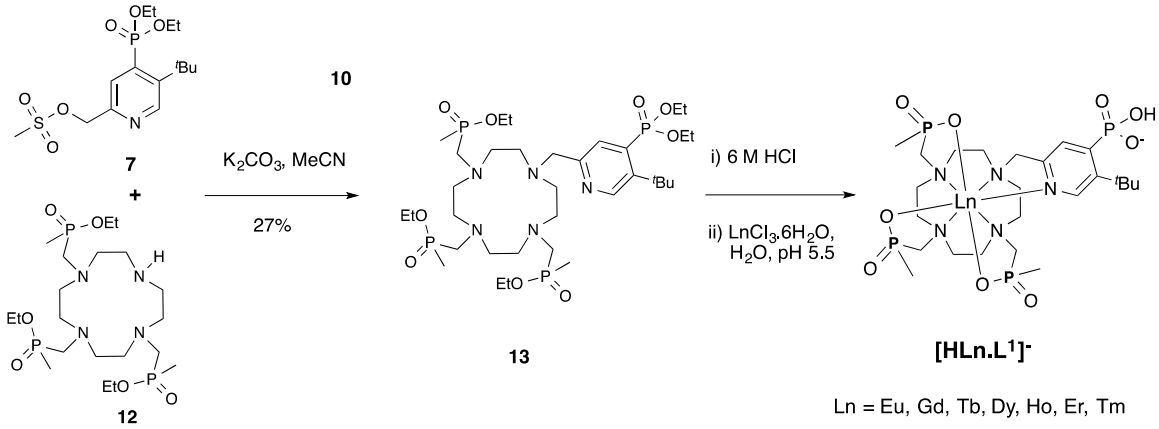


**Scheme 3**

## Characterisation of 6

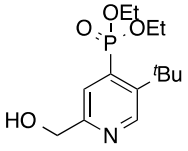

**$^1$H NMR (400 MHz, $CDCl_3$, 295 K):**

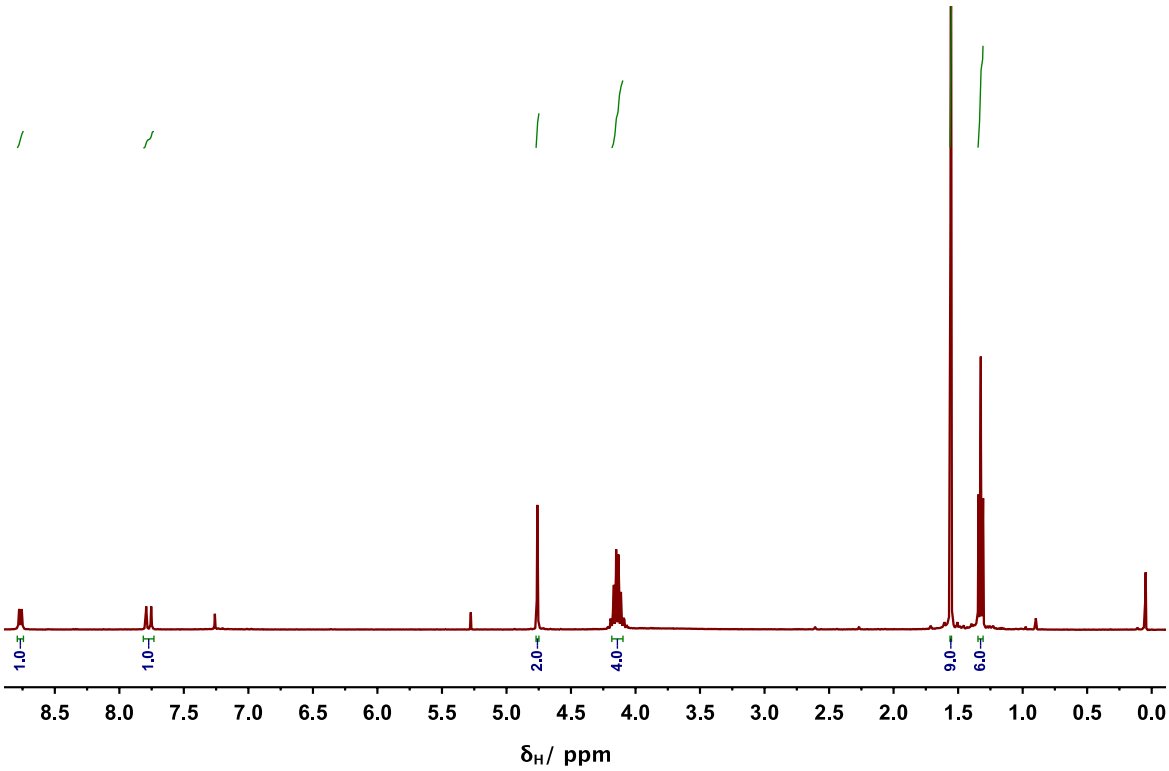


**$^{31}$P NMR (162 MHz, $CDCl_3$, 295 K):**

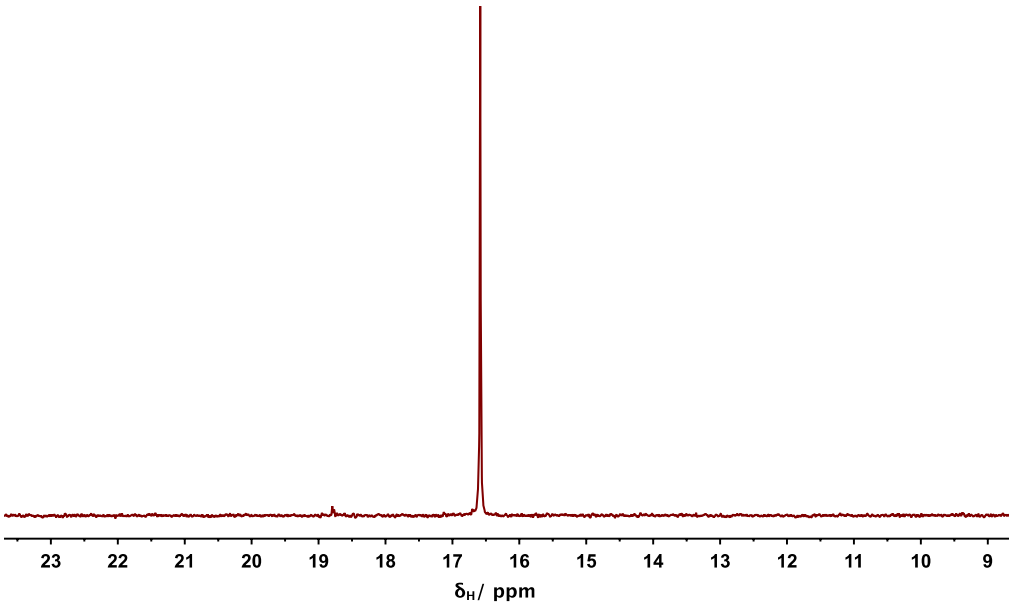


**$^{13}$C NMR (101 MHz, $CDCl_3$, 295 K):**

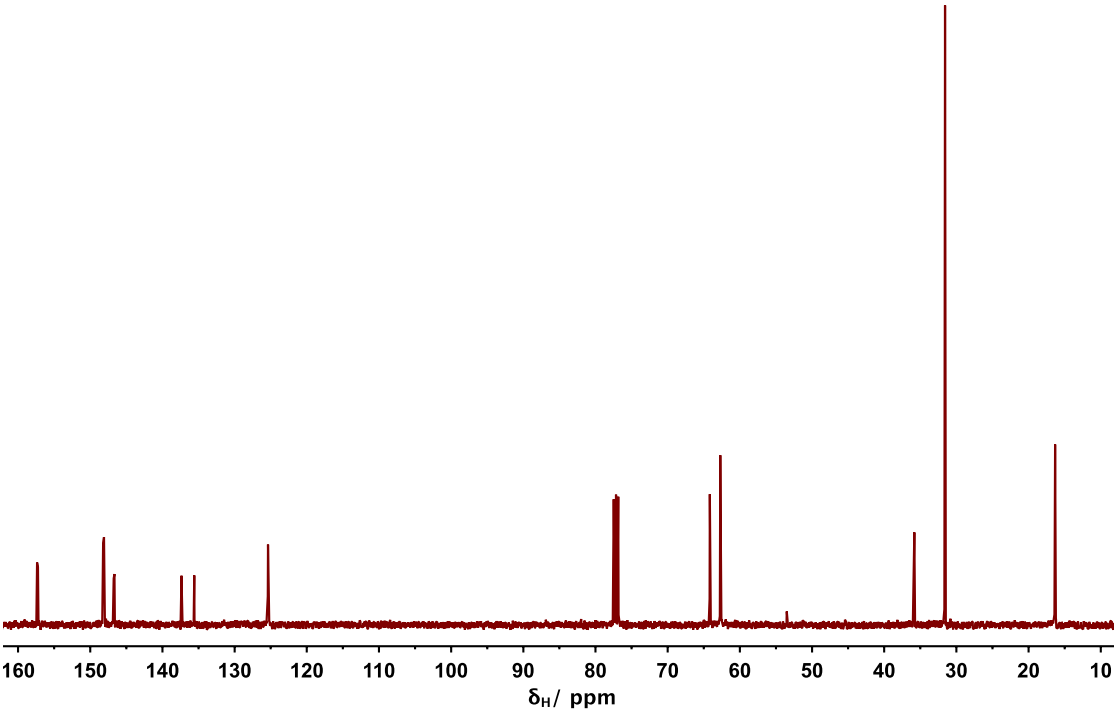
160
150
140
130
120
110
100
90
80
70
60
50
40
30
20
10
δH/ ppm